

# Raman Spectroscopy as a Key Method to Distinguish the Ferroelectric Orthorhombic Phase in Thin ZrO<sub>2</sub>-Based Films

Monica Materano,\* Peter Reinig, Alfred Kersch, Maxim Popov, Marco Deluca, Thomas Mikolajick, Ulrich Boettger, and Uwe Schroeder

Inducing and detecting the polar orthorhombic phase are crucial for the establishment of ferroelectricity in HfO<sub>2</sub>- and ZrO<sub>2</sub>-based thin films. Unfortunately, commonly used structural characterization techniques such as grazing incidence angle X-ray diffraction (GIXRD) only partially allow an accurate detection of this crystalline phase, whose characteristic pattern almost coincides with the one of the tetragonal phase. As a consequence, phase determination is commonly based on peak deconvolution tracing the position of the main peak at 2θ values of around 30°, which can be assigned both to the t(101) and the o(111) plane directions and additionally be influenced by mechanical stress in the layers. Alternatively, epitaxial layers are required to differentiate the phase. Herein, using an integrated experimental–computational approach, it is shown how Raman spectroscopy can distinguish between the monoclinic, the tetragonal, and the orthorhombic phase of ZrO<sub>2</sub>. The Raman spectra calculated from first principles match the experimentally measured data and thus enable an unambiguous phase assignment. Therefore, Raman spectroscopy proves to be a powerful technique for discerning the three main crystalline phases in these materials. As demonstrated by the good agreement between structural and electrical data, it can therefore be used to predict ferroelectricity in the addressed layers.

reasonably high dielectric constants.<sup>[1,2]</sup> These properties, together with the already explored integration routes in current semiconductor process flows, made them exceptional candidates not only for high-k gate stacks applications<sup>[3]</sup> but also in traditional and emerging memory concepts such as DRAM<sup>[4]</sup> and RRAM.<sup>[5]</sup> Ferroelectricity was first reported in HfO<sub>2</sub> thin films in 2011,<sup>[6]</sup> when Böscke et al. correlated the appearance of a remanent polarization ( $P_r$ ) to the presence of a non-centrosymmetric polar orthorhombic (o-) phase with space group Pca21. Shortly after that, similar findings were reported in mixed oxides of hafnium and zirconium<sup>[7]</sup> and in ZrO<sub>2</sub>.<sup>[8]</sup> The polar phase seemed to be only stabilized over the more common monoclinic (m-) and tetragonal (t-) phases (with space groups P21/c and P42/nmc, respectively) through particular nonequilibrium conditions. Optimized oxygen content,<sup>[9]</sup> introduction of a dopants,<sup>[10]</sup> rapid quenching,<sup>[11]</sup> high pressure,<sup>[12]</sup> surface energy,<sup>[13]</sup> mechanical stress,<sup>[14]</sup>

## 1. Introduction


In the last decades, the interest in hafnia- and zirconia-based materials has experienced a tremendous growth in the field of micro- and nanoelectronics, thanks to numerous exiting properties. As a matter of fact, HfO<sub>2</sub>, ZrO<sub>2</sub>, and their mixed solution present good thermal stability, relatively wide bandgap, and

and electric field<sup>[15]</sup> were all suggested in the past years as levers for the establishment of ferroelectricity, i.e., the stabilization of the polar orthorhombic phase in HfO<sub>2</sub>- and ZrO<sub>2</sub>-based thin films. Contrarily to HfO<sub>2</sub>, ZrO<sub>2</sub> allows the stabilization of the polar orthorhombic phase in films of higher thickness.<sup>[16–18]</sup> Among the techniques used to characterize the crystalline phase of thin films structurally, grazing incidence angle X-ray

M. Materano, T. Mikolajick, U. Schroeder  
 NaMLab gGmbH  
 Noethnitzer Strasse 64a, 01187 Dresden, Germany  
 E-mail: monicamaterano@gmail.com, uwe.schroeder@namlab.com

P. Reinig  
 Fraunhofer Institut für Photonische Mikrosysteme (IPMS)  
 Maria-Reiche-Straße 2, 01109 Dresden, Germany

A. Kersch  
 Hochschule München  
 Lothstr. 34, 80335 München, Germany

 The ORCID identification number(s) for the author(s) of this article can be found under <https://doi.org/10.1002/pssr.202100589>.

DOI: 10.1002/pssr.202100589

M. Popov, M. Deluca  
 Materials Center Leoben Forschung GmbH (MCL)  
 Roseggerstrasse 12, AT 8700 Leoben, Austria

T. Mikolajick  
 Chair of Nanoelectronic Materials  
 TU Dresden  
 Noethnitzer Strasse 64, 01062 Dresden, Germany

U. Boettger  
 RWTH Aachen  
 Templergraben 55, 52062 Aachen, Germany

diffraction (GIXRD) is certainly the most used. Thanks to the low penetration depth allowed by the small incidence angles used within this method, films in the nm thickness range can be measured, and their phase effectively deconvoluted. Nonetheless, the X-ray diffraction (XRD) patterns of the orthorhombic and the tetragonal phase present their main features at similar  $2\theta$  values, making the distinction of the two crystalline phases extremely tricky. In particular, the main intensity peak of the orthorhombic phase of the (111) plane is indexed at  $2\theta = 30.4^\circ$ , whereas the one of the tetragonal phases in the (101) plane is indexed at  $2\theta = 30.8^\circ$ . However, it was often reported that the position of this main feature could vary in the presence of a mechanical stress in the layer,<sup>[19]</sup> making phase discernment even more complicated. In the past, several groups managed to detect a high-pressure orthorhombic phase in HfO<sub>2</sub> and ZrO<sub>2</sub> single crystals, ribbons, and powders by means of Raman spectroscopy.<sup>[20–22]</sup> Phase transition from the tetragonal/cubic to the monoclinic phase or from an amorphous to a crystalline state because of high imposed temperatures was also reported.<sup>[23,24]</sup> Othaka et al. detected a transition from the m- to an orthorhombic phase by means of high pressure and Y doping of ZrO<sub>2</sub>.<sup>[25]</sup> Nonetheless, the orthorhombic phase was not correlated to electrical polarization, and ferroelectricity in fluorite materials had by that time not been reported yet. Furthermore, there are no theoretical predictions of the Raman features corresponding to the assigned crystalline phases that accompanied the experimental findings in the cited reports. In this work, we fabricate thin ferroelectric ZrO<sub>2</sub> films and use Raman Spectroscopy as the main structural characterization technique for phase determination. Zirconia films were preferred for this study because their interval for the stabilization of the ferroelectric phase is shifted to higher thicknesses as compared to hafnia layers. A larger thickness was necessary in order to obtain a reasonable signal-to-noise ratio for the Raman measurements. In addition, we deploy density functional theory (DFT) calculations to simulate the expected Raman spectra of ZrO<sub>2</sub> phases and compare them to the measured ones. We demonstrate how both simulations and experimentally obtained Raman features well compare to GIXRD results and ultimately to the electrically measured ferroelectric performance of the films. Last but not least, a variation in the Raman spectrum after applying an external electric field is used to support the hypothesis of a possible field-induced phase transition in ZrO<sub>2</sub>-based capacitors.

## 2. Results and Discussion

### 2.1. Calculation of the Raman Spectra from Ab Initio

The Raman intensity spectrum was calculated from ab initio. The calculation is challenging for two reasons. First, the phonon modes in polar crystals are simultaneously infrared and Raman active, which essentially doubles the number of Raman active modes. Furthermore, the Raman modes are subject to longitudinal optical–transverse optical (LO–TO) splitting,<sup>[26]</sup> which again increases the number contributions to the intensity spectrum. To estimate the theoretical error in the Raman spectrum, two different calculation methods were used.

In the first approach, an ABINIT implementation of the DFT was used, together with density functional perturbation theory (DFPT)<sup>[27]</sup> based on projector augmented wave (PAW) pseudopotentials from the GBRV library.<sup>[28]</sup> The local density approximation was chosen as it often gives better values for vibrational frequencies in metal oxides than functionals based on the gradient-corrected approximation.<sup>[29]</sup> The calculation was based on the previously determined lattice constants. The LO–TO splitting from long-range electrostatic interaction was considered with the analytical formula implemented in ABINIT, and the resulting peaks were simply added.

In the second approach, the Raman spectra were computed according to the spherical averaging method<sup>[30]</sup> using the Vienna Ab initio Simulation Package (VASP) code<sup>[31]</sup> for DFT calculations. The electron–ion interactions were described within the framework of PAWs,<sup>[32]</sup> while the exchange–correlation effects were treated at the Perdew–Burke–Ernzerhof functional revised for solids (PBEsol)<sup>[33]</sup> level of theory. The experimental lattice parameters of the considered phases of zirconia were used. The phonon calculations were performed using the Phonopy code.<sup>[34]</sup> Details of method 1 and method 2 are described in the Supporting Information.

The Raman intensity of an oriented crystal depends on the frequency of the incident laser and the temperature of the sample. In a polycrystalline sample, the summation over all possible orientations in the Placzek approximation<sup>[35]</sup> leads to an algebraic expression containing the rotational invariants  $G(0)$ ,  $G(1)$ , and  $G(2)$  of the Raman tensor. It is important to note that the Raman intensity does not depend on the direction of polarization in the crystal. The Raman intensity is therefore not sensitive to the average polarization, but only to the phase content of the polar phase. The formula for the polarized intensity is collected in the Supporting Information. Furthermore, the Supporting Information contains the detailed computational results and a comparison of calculated and literature experimental data for the tetragonal and monoclinic phase. For the polar orthorhombic (Pca21), tetragonal (P21/c), and monoclinic (P42/nmc) ZrO<sub>2</sub> crystal structures, the phonon frequencies were calculated at the  $\Gamma$ -point. The assignment of the modes as being Raman active or infrared active was apparent from the Raman tensor or oscillation strength being nonzero. The assignment was verified with the group theoretical symmetry analysis of the Raman tensor from the Bilbao Crystallographic Server.<sup>[36]</sup> In the centrosymmetric crystals, the modes are either Raman active or infrared active. In noncentrosymmetric crystals, modes can be simultaneously Raman and infrared active. **Table 1** summarizes the Raman modes with the largest intensity of the polar orthorhombic, tetragonal, and monoclinic phase, which can be compared with intensity maxima from the experiment. A table with all modes is provided in Table S1–S3, Supporting Information.

**Figure 1** shows the calculated Raman spectrum calculated with the two presented methods. For wavenumber above  $140\text{ cm}^{-1}$ , intense tetragonal peaks are calculated for  $143$ ,  $266$ ,  $322$ ,  $463$ ,  $598$ , and  $648\text{ cm}^{-1}$ . Intense polar orthorhombic peaks are calculated for  $199$ ,  $309$ ,  $341$ ,  $545$ , and  $579\text{ cm}^{-1}$ . Intense monoclinic peaks, which should be unaffected by an electric field, are expected for  $183$ ,  $225$ ,  $389$ ,  $470$ , and  $611\text{ cm}^{-1}$ . A comparison between method 1 and method 2 results in minimal

**Table 1.** Comparison of the experimental Raman peak positions with calculated modes of medium and high intensity. The experimental peaks are assigned to the polar phase when the intensity increases with cycling relative to the pristine peak, otherwise to the tetragonal phase. The values are in  $\text{cm}^{-1}$ .

| Polar orthorhombic |          |          | Tetragonal |          |          | Monoclinic |          |          |
|--------------------|----------|----------|------------|----------|----------|------------|----------|----------|
| Exp.               | Method 1 | Method 2 | Exp.       | Method 1 | Method 2 | Exp.       | Method 1 | Method 2 |
| 200                | 193–199  | 179–191  | 145        | 143      | 139      | 185        | 183–192  | 178–186  |
| ?                  | 309      | 286      | 273        | 266      | 272      | ?          | 225      | 221      |
| 320                | 341      | 316      | 320        | 322      | 314      | ?          | 320      | 318      |
| 340                | 366      | 339      | 460        | 463      | 446      | 378        | 389      | 381      |
| ?                  | 401      | 381      | 600        | 598      | 586      | 465        | 470      | 457      |
| ?                  | 458      | 437      | 650        | 648      | 646      | 552        | 552      | 551      |
| 550                | 545      | 522      |            |          |          |            | 611      | 606      |
| 580                | 579      | 558      |            |          |          |            | 636      | 635      |
| 620                | 620      | 607      |            |          |          |            |          |          |

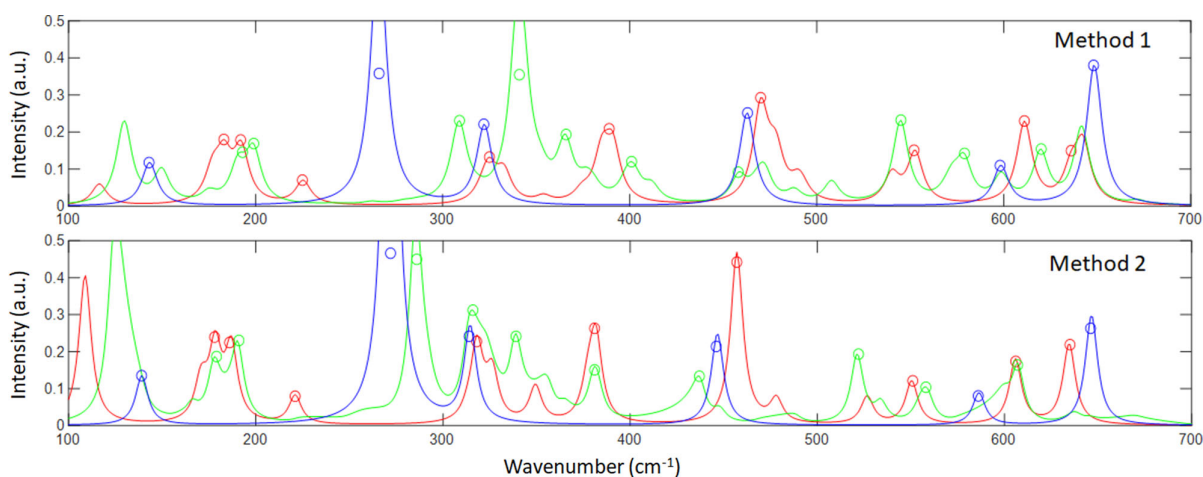


**Figure 1.** Total Raman intensities calculated with method 1 and method 2 for the tetragonal (blue), polar orthorhombic (green), and monoclinic (red) phases. The symbols (circles) indicate the most intense peaks, which are listed in Table 1.

differences between the calculated Raman shifts corresponding to the same vibrational modes. A detailed explanation is supplied in Table S4, Supporting Information.

## 2.2. Raman Spectroscopy for Phase Determination: A Comparison with GIXRD

A 100 nm-thick  $\text{ZrO}_2$  layer was deposited via chemical solution deposition (CSD).<sup>[18,37]</sup> As a starting point, a GIXRD pattern of a 100 nm-thick film was measured as reported in Figure 2a. Rietveld refinement allowed the calculation of a m-phase portion of about 21% and a o/t-phase content of about 79% (see Table 2). Compared to former reports,<sup>[38]</sup> the t- and o-phase were difficult to distinguish by Rietveld. Similar phase fractions were determined when a t- or o-phase was assumed. Accordingly, an overall o/t-phase content is reported. In addition, Raman measurements were performed (Figure 2b) and compared to the Raman simulation results discussed above. Method 1 delivered Raman shifts closer to the experimentally observed values and was therefore

used for comparison (see Table S4, Supporting Information). The strongest peaks can be attributed to high t-phase portions. Smaller features fit nicely to monoclinic portions, but minor o-phase portion might be present. This is the case for the peaks at 183, 225, 389, and 470  $\text{cm}^{-1}$ , associated to the m-phase and for those at 199, 309, 341, 545, and 579, linked to the o-phase, and 143, 266, 322, 463, 598, and 648  $\text{cm}^{-1}$  attributed to the t-phase (see Table 1).

In the literature, Raman results for the polar o-phase are not discussed, but m- to t-portions are determined<sup>[39,40]</sup> by comparing the intensity of the main peaks corresponding to the m- and t-phase. A similar calculation was performed for the experimental measurements shown in Figure 2b, and the results are shown in Table 2, where a comparison with the GIXRD-calculated m-phase content shows exceptional agreement between the two results, indicating a m-phase content of about 22% and t-phase portions of 78%.

Furthermore, polarization hysteresis measurements were performed on capacitor structures with Pt electrodes. In the pristine state, a pinched hysteresis loop is observed (Figure 3), indicating a remanent polarization of about  $2 \mu\text{C cm}^{-2}$  without external bias

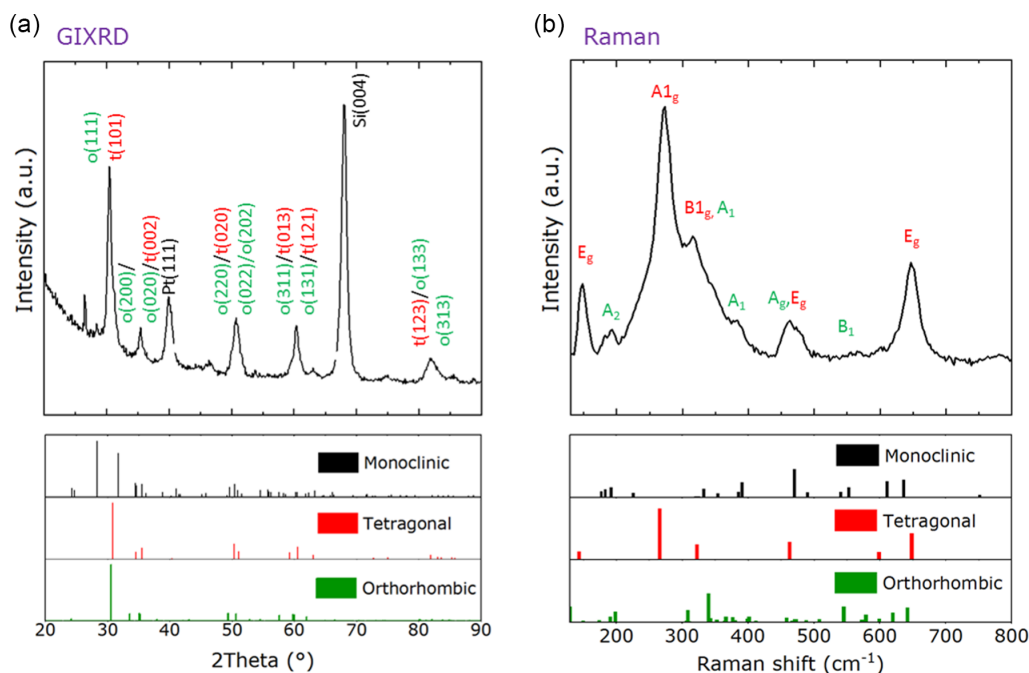


**Figure 2.** Experimentally measured a) GIXRD and b) Raman patterns for a pristine CSD-deposited  $\text{ZrO}_2$  layer. The Raman measurement was performed between capacitors, directly on the  $\text{ZrO}_2$  layer. The main features belonging to the m-, t-, and polar o-phase are tagged. As a reference, in the underlying panels the theoretical (PDF Cards) and the simulated (this work, method 1) main peaks are reported for GIXRD and Raman spectroscopy, respectively.

**Table 2.** m- and t/o-phase content calculated from the Raman<sup>[39]</sup> and GIXRD measurements for a pristine CSD-deposited  $\text{ZrO}_2$  layer.

|       | m-Phase content [%] | t/o-Phase content [%] |
|-------|---------------------|-----------------------|
| Raman | 22                  | 78                    |
| GIXRD | 21                  | 79                    |

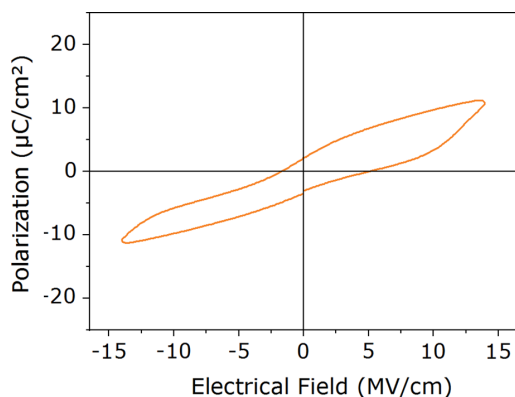


**Figure 3.** Polarization as a function of the applied field for a CSD-deposited  $\text{ZrO}_2$  layer in the pristine state.

field. The application of a bias field of  $14 \text{ MV cm}^{-1}$  is assumed to cause a field-induced phase change to the polar o-phase leading to a saturation polarization of  $12 \text{ } \mu\text{C cm}^{-2}$ . Assuming a polycrystalline  $\text{HfO}_2$  or  $\text{ZrO}_2$  layer with random orientation of crystallites, typically, a maximum remanent polarization of  $26 \text{ } \mu\text{C cm}^{-2}$

is reported for nontextured films.<sup>[9]</sup> By considering the pristine  $P_r$  of  $2 \text{ } \mu\text{C cm}^{-2}$ , this would mean that 10% of the layer is in the polar o-phase in its initial unbiased state. After applying an electrical field, about 50% of the layer can be transformed to the polar phase. This is in very good agreement with the results indicated by the Raman measurement for the pristine sample.

### 2.3. Detection of a Field-Induced Phase Transition

In a second step, a 30 nm-thick  $\text{ZrO}_2$  capacitor was fabricated utilizing ALD. Five cycles  $\text{Al}_2\text{O}_3$  were introduced after the first 15 nm  $\text{ZrO}_2$  to avoid stabilizing the m-phase for bulk  $\text{ZrO}_2$  and promote ferroelectricity. The GIXRD pattern for the fabricated structure is reported in **Figure 4a**. Only a small portion of m-phase is detected, whereas most of the film crystallized in the t/o-phase. A Gaussian deconvolution of the spectra resulted in 14%, 59%, and 27% of m-, o-, and t-phase, respectively, assuming a fixed o(111)  $2\theta$  value at  $30.4^\circ$  or a t(101) position at  $30.8^\circ$ . Values were taken from former measurements.<sup>[9]</sup> But a Gaussian deconvolution assumes a constant stress in the layer, which is an arbitrary assumption.

**Figure 5b** reports the current versus field performance of the addressed capacitor for increasing externally applied fields. As seen in the graph, two distinct switching peaks are present at low fields which later merge into one single switching feature for larger applied fields, confirming the establishment of a polar phase and therefore of ferroelectricity for higher applied fields already during the first switching cycle. In order to understand if a polar o-phase is already entirely present in the layer in the as-deposited state or if it partially arises because of field-induced

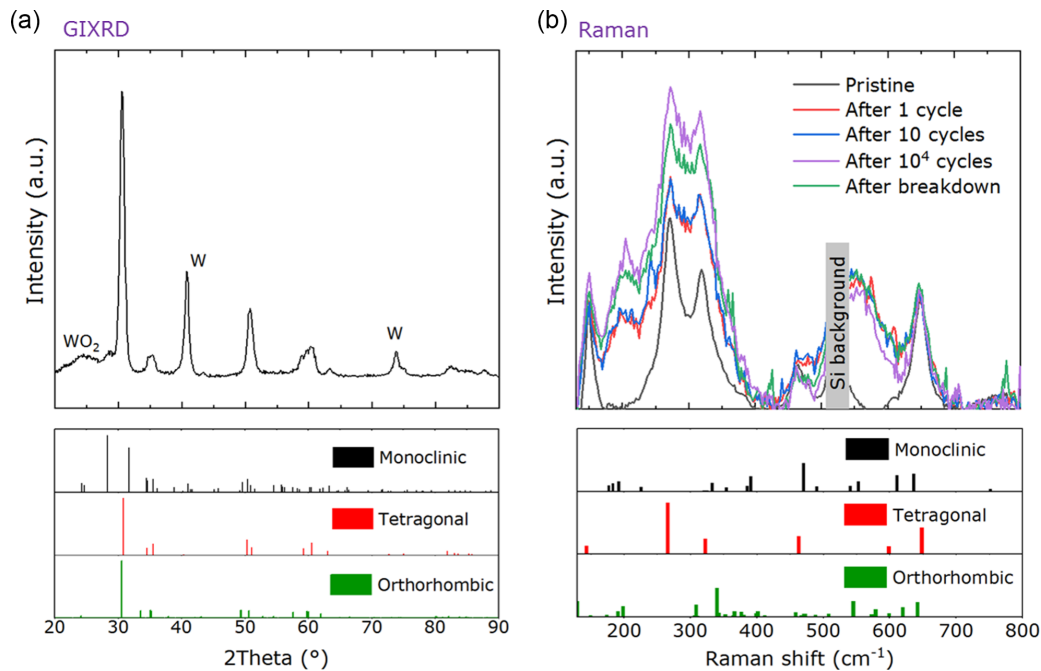


**Figure 4.** Experimentally measured a) GIXRD and b) Raman spectra for an atomic layer deposition (ALD)-deposited  $\text{ZrO}_2$  layer. Raman measurements were performed through the top electrode in order to address single capacitor structures. As a reference, in the underlying panels, the theoretical (PDF Cards) and the simulated (this work, method 1) main peaks are reported for GIXRD and Raman spectroscopy, respectively. The Raman measurements were performed after different device cycling stages. The spectra were normalized with respect to the Si background peak.

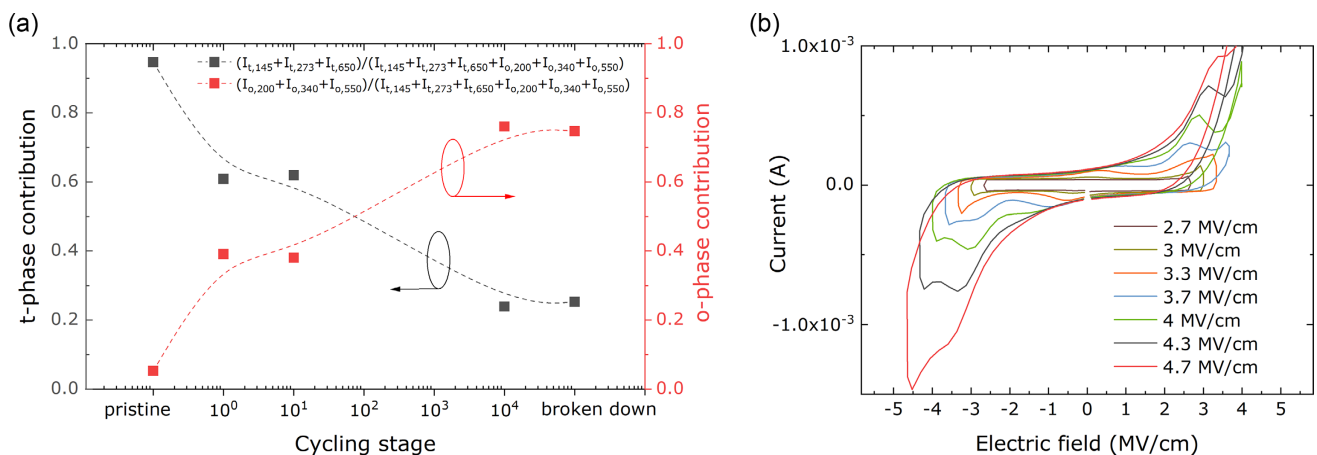


**Figure 5.** a) t- and o-phase contributions calculated in a similar fashion as described in the study by Clarke and Adar<sup>[39]</sup> for capacitors after a different amount of field cycling and b) current versus electric field for different applied electric fields for an ALD-deposited  $\text{ZrO}_2$  layer.

phase transition, Raman measurements were performed on capacitors in the pristine state and after 1, 10, and 10 000 cycles. One last measurement was taken after hard dielectric breakdown. The results are displayed in Figure 4b, and the features are tagged referring to the simulated Raman patterns. The spectra were normalized with respect to the background Si peak and method 1 was used for comparison. A decrease in intensity is observed for the features at 145, 273, 460, and 650  $\text{cm}^{-1}$ , which belong to the t-phase. On the other hand, the intensity of the peaks at 200, 340, and 550  $\text{cm}^{-1}$  rises with increasing number of applied field cycles, indicating a field-induced phase transition

from the t- to the o/m-phase. Similar to the CSD  $\text{ZrO}_2$  case, the ratio between the intensity of the main features belonging to the t- and to the m/o-phase was monitored. Checking the cycling stage of the device, a sudden drop in the t-phase contribution is detected already after the application of the first field cycle, which further drops at a lower rate from that stage onward. The opposite behavior is observed for the polar o-phase contribution, as displayed in Figure 5a), where phase contributions and trends with respect to the cycling stage are estimated in a similar fashion as presented in the study by Clarke and Adar.<sup>[39]</sup> This possibly indicates a field-induced phase transition

already taking place within the first voltage application. Again, XRD measurements could not clearly distinguish o- versus t-phase content, but now Raman clearly revealed phase changes during cycling, indicating a t- to o-phase transition (Figure 4b) and Figure 5a)). Accordingly, Raman spectroscopy can give new insights into phase characterization of doped HfO<sub>2</sub> or ZrO<sub>2</sub>, also supporting the in situ characterization of thin-film capacitors.

### 3. Conclusions

In this work, the potential of Raman spectroscopy in enabling the distinction of the o- and the t-phase in thin, ferroelectric ZrO<sub>2</sub> films was demonstrated. First, Raman spectra were simulated via ab initio calculations for the monoclinic, the polar orthorhombic, and the tetragonal phase in ZrO<sub>2</sub> with two different methods. It was shown how each crystalline phase possesses a certain number of unique features, which enable phase detection in a more clear way as compared to GIXRD, where the main polar orthorhombic and tetragonal peaks overlap. Then, the calculated patterns were compared to experimental data collected for CSD- and ALD-deposited ZrO<sub>2</sub> films. Results were compared with the more common GIXRD analysis, showing good agreement between the two methods. Field cycles were imposed to single capacitor structures and phase was monitored at different device lifetime stages via Raman spectroscopy. Trends in phase contributions could be observed with respect to the capacitor cycling stage. A field-induced phase transition from the tetragonal to the polar phase with increasing field cycling was confirmed both via Raman and electrical measurement.

### 4. Experimental Section

ZrO<sub>2</sub> layers were deposited via CSD and ALD. For the CSD-deposited films, the precursor solution consisted of zirconium 2,4-pentadionate dissolved in propionic acid and propionic acid anhydrite (5:3) at 140 °C for 6 h and subsequently spin-coated on a 100 nm-thick platinum bottom electrode with a (111) orientation. After each spin coating, samples were heated at 215 °C for 5 min. The desired film thickness was achieved by repeating the spin coating step. A rapid thermal processing step at 800 °C for 90 s in an argon/oxygen atmosphere (1:1) was performed to finalize crystallization. ALD-based capacitors were fabricated by sandwiching a 30 nm ZrO<sub>2</sub> layer split in two 15 nm halves by a five ALD cycles thick Al<sub>2</sub>O<sub>3</sub> layer between a W/TiN bottom electrode and a TiN top electrode. CpZr[N(CH<sub>3</sub>)<sub>2</sub>]<sub>3</sub> (ZyALD), (CH<sub>3</sub>)<sub>3</sub>Al (TMA), and O<sub>3</sub> were used as Zr, Al, and oxygen source, respectively. A minimum thickness of 30 nm was required in order to obtain reasonable Raman intensity. The deposition temperature was set at 350 °C in order to promote crystallization already during deposition. Both top and bottom electrodes were deposited via physical vapor deposition. Sample thickness was measured by X-ray reflectivity with a Bruker D8 Discover XRD Tool using a Cu K $\alpha$  source. The crystalline phase was estimated via GIXRD on the same tool. Raman measurements were performed at room temperature with a confocal Raman microscope tool (Renishaw inVia Qontor) confocal microscope tool with a continuous wave (cw) laser (TEM<sub>00</sub>, polarization ratio 100:1, vertical) of 405 nm wavelength using a Leica DM2700 microscope with NPLAN-objective lens (100 $\times$ ). The spectral resolution of the system is <1 cm<sup>-1</sup> full width at half maximum (FWHM). Measurements were conducted in Stokes regime using a Rayleigh filter with 100 cm<sup>-1</sup> cutoff wavenumber. Laser output power at 405 nm was set to 3 mW and sample illumination was performed in parallel to the film surface normal. Integration time of a single spectral measurement was 1200 s and

displayed spectra represent the integration of three subsequent single measurements (i.e., total 3600 s measurement time per spectrum). The measurements at 405 nm wavelength turned out to be superior compared to additional measurements at 532 and 785 nm to achieve a suitable signal-to-noise ratio while avoiding detrimental effects on the spectra due to the underlying silicon substrate peak. Measurements were performed directly on the ZrO<sub>2</sub> layer for the CSD-deposited sample and through the top electrode for the ALD-deposited ones. This was done in order to address single capacitor structures and monitor phase evolution with field cycling. Polarization versus electric field (P-E) hysteresis measurements were performed with an aixACCT Systems TF Analyzer 3000 using a measurement frequency of 1 kHz, whereas cycling was conducted at a frequency of 100 kHz.

### Supporting Information

Supporting Information is available from the Wiley Online Library or from the author.

### Acknowledgements

M.M. would like to thank Sony Corporation for funding. A.K. gratefully acknowledges the Gauss Centre for Supercomputing e.V. (www.gauss-centre.eu) for funding this project by providing computing time on the GCS Supercomputer SuperMUC-NG at Leibniz Supercomputing Centre (www.lrz.de) under grant: pr27su. Part of this work was financially supported out of the state budget approved by the delegates of the Saxon State parliament. M.N.P. and M.D. received funding from the European Research Council (ERC) under the European Union's Horizon 2020 research and innovation program (grant agreement no. 817190). The work of P.R. was partly funded by the Federal Ministry of Education and Research (BMBF) under the project reference numbers 16FMD01K, 16FMD02, and 16FMD03.

### Conflict of Interest

The authors declare no conflict of interest.

### Data Availability Statement

The data that support the findings of this study are available from the corresponding author upon reasonable request.

### Keywords

crystalline phases, ferroelectricity, phase transition, Raman spectroscopy, zirconium oxide

Received: November 26, 2021  
Revised: December 10, 2021  
Published online: January 19, 2022

- [1] H. Harris, K. Choi, N. Mehta, A. Chandolu, N. Biswas, G. Kipshidze, S. Nikishin, S. Gangopadhyay, H. Temkin, *Appl. Phys. Lett.* **2002**, *81*, 1065.
- [2] Y.-S. Lin, R. Puthenkovilakam, J. P. Chang, *Appl. Phys. Lett.* **2002**, *81*, 2041.
- [3] M. Bohr, R. Chau, T. Ghani, K. Mistry, *IEEE Spectr.* **2007**, *44*, 29.

- [4] A. Berthelot, C. Caillat, V. Huard, S. Barnola, B. Boeck, H. Del-Puppo, N. Emonet, F. Lalanne, in *2006 European Solid-State Device Research Conf.*, IEEE, Montreux, Switzerland **2006**, p. 343.
- [5] B. Govoreanu, G. S. Kar, in *Int. Electron Devices Meeting 2011*, IEEE, Washington, DC, USA **2011**.
- [6] T. S. Böske, J. Müller, D. Bräuhaus, U. Schröder, U. Böttger, *Appl. Phys. Lett.* **2011**, 99, 102903.
- [7] J. Müller, T. S. Böske, D. Bräuhaus, U. Schröder, U. Böttger, J. Sundqvist, P. Kücher, T. Mikolajick, L. Frey, *Appl. Phys. Lett.* **2011**, 99, 112901.
- [8] B.-T. Lin, Y.-W. Lu, J. Shieh, M.-J. Chen, *J. Eur. Ceram. Soc.* **2017**, 37, 1135.
- [9] M. Materano, T. Mittmann, P. D. Lomenzo, C. Zhou, J. L. Jones, M. Falkowski, A. Kersch, T. Mikolajick, U. Schroeder, *ACS Appl. Electron. Mater.* **2020**, 2, 3618.
- [10] U. Schroeder, E. Yurchuk, J. Müller, D. Martin, T. Schenk, P. Polakowski, C. Adelman, M. I. Popovici, S. V. Kalinin, T. Mikolajick, *Jpn. J. Appl. Phys.* **2014**, 53, 08LE02.
- [11] A. Toriumi, L. Xu, Y. Mori, X. Tian, P. D. Lomenzo, H. Mulaosmanovic, M. Materano, T. Mikolajick, U. Schroeder, in *Int. Electron Devices Meeting*, San Francisco **2019**.
- [12] B. Buyantogtokh, V. Gaddam, S. Jeon, *J. Appl. Phys.* **2021**, 129, 244106.
- [13] M. H. Park, Y. H. Lee, H. J. Kim, T. Schenk, W. Lee, K. D. Kim, F. P. G. Fengler, T. Mikolajick, U. Schroeder, C. S. Hwang, *Nanoscale* **2017**, 9, 9973.
- [14] H. Joh, T. Jung, S. Jeon, *IEEE Trans. Electron Devices* **2021**, 68, 2538.
- [15] P. D. Lomenzo, T. Mikolajick, U. Schroeder, in *IEEE Int. Symp. on Applications of Ferroelectric (ISAF)*, IEEE, Piscataway, NJ **2021**, p. 4.
- [16] M. Materano, C. Richter, T. Mikolajick, U. Schroeder, *J. Vac. Sci. Technol. A* **2020**, 38, 022402.
- [17] R. Materlik, C. Künneth, A. Kersch, *J. Appl. Phys.* **2015**, 117, 134109.
- [18] S. Starschich, T. Schenk, U. Schroeder, U. Boettger, *Appl. Phys. Lett.* **2017**, 110, 182905.
- [19] M. Hyuk Park, H. Joon Kim, Y. Jin Kim, T. Moon, C. Seong Hwang, *Appl. Phys. Lett.* **2014**, 104, 072901.
- [20] H. Arashi, M. Ishigame, *Phys. Status Solidi A* **1982**, 71, 313.
- [21] H. Arashi, *J. Am. Ceram. Soc.* **1992**, 75, 844.
- [22] G. Mandal, R. Jana, P. Saha, P. Das, *Mater. Today Proc.* **2016**, 3, 2997.
- [23] M. Li, Z. Feng, G. Xiong, P. Ying, Q. Xin, C. Li, *J. Phys. Chem. B* **2001**, 105, 8107.
- [24] M. Modreanu, J. Sancho-Parramon, O. Durand, B. Servet, M. Stchakovsky, C. Eypert, C. Naudin, A. Knowles, F. Bridou, M.-F. Ravet, *Appl. Surf. Sci.* **2006**, 253, 328.
- [25] O. Ohtaka, S. Kume, T. Iwami, K. Urabe, *J. Am. Ceram. Soc.* **1988**, 71, C.
- [26] R. Durman, P. Favre, U. A. Jayasooriya, S. F. A. Kettle, *J. Crystallogr. Spectrosc. Res.* **1987**, 17, 431.
- [27] X. Gonze, B. Amadon, G. Antonius, F. Arnardi, L. Baguet, J.-M. Beuken, J. Bieder, F. Bottin, J. Bouchet, E. Bousquet, N. Brouwer, F. Bruneval, G. Brunin, T. Cavignac, J.-B. Charraud, W. Chen, M. Côté, S. Cottenier, J. Denier, G. Geneste, P. Ghosez, M. Giantomassi, Y. Gillet, O. Gingras, D. R. Hamann, G. Hautier, X. He, N. Helbig, N. Holzwarth, Y. Jia, et al., *Comput. Phys. Commun.* **2020**, 248, 107042.
- [28] K. F. Garrity, J. W. Bennett, K. M. Rabe, D. Vanderbilt, *Comput. Mater. Sci.* **2014**, 81, 446.
- [29] X. Zhao, D. Vanderbilt, *Phys. Rev. B* **2002**, 65, 233106.
- [30] M. N. Popov, J. Spitaler, V. K. Veerapandian, E. Bousquet, J. Hlinka, M. Deluca, *Npj Comput. Mater.* **2020**, 6, 121.
- [31] G. Kresse, J. Furthmüller, *Phys. Rev. B* **1996**, 54, 11169.
- [32] G. Kresse, D. Joubert, *Phys. Rev. B* **1999**, 59, 1758.
- [33] J. P. Perdew, A. Ruzsinszky, G. I. Csonka, O. A. Vydrov, G. E. Scuseria, L. A. Constantin, X. Zhou, K. Burke, *Phys. Rev. Lett.* **2008**, 100, 136406.
- [34] A. Togo, I. Tanaka, *Scr. Mater.* **2015**, 108, 1.
- [35] R. Caracas, *J. Chem. Phys.* **2007**, 127, 144510.
- [36] M. I. Aroyo, J. M. Perez-Mato, C. Capillas, E. Kroumova, S. Ivantchev, G. Madariaga, A. Kirov, H. Wondratschek, *Z. Kristallogr. Cryst. Mater.* **2006**, 221, 15.
- [37] U. Böttger, S. Starschich, D. Griesche, T. Schneller, in *Ferroelectricity in Doped Hafnium Oxide: Materials, Properties and Devices* (Eds: U. Schroeder, C. S. Hwang, H. Funakubo), Woodhead Publishing, Sawston **2019**, p. 127.
- [38] M. H. Park, T. Schenk, C. M. Fancher, E. D. Grimley, C. Zhou, C. Richter, J. M. LeBeau, J. L. Jones, T. Mikolajick, U. Schroeder, *J. Mater. Chem. C* **2017**, 5, 4677.
- [39] D. R. Clarke, F. Adar, *J. Am. Ceram. Soc.* **1982**, 65, 284.
- [40] S. N. Tkachev, M. H. Manghnani, A. Niilisk, J. Aarik, H. Mändar, *Spectrochim. Acta, Part A* **2005**, 61, 2434.